RSC Advances

PAPER

View Article Online
View Journal | View Issue

Cite this: *RSC Adv.*, 2024, **14**, 3335

Investigation of the structure and dielectric properties of doped barium titanates

Mohamed M. Salem,*[a] Moustafa A. Darwish,*[a] Aseel M. Altarawneh,[a] Yamen A. Alibwaini,[ab] Ryad Ghazy,[a] Osama M. Hemeda,[a] Di Zhou,[c] Ekaterina L. Trukhanova,[de] Alex V. Trukhanov,[de] Sergei V. Trukhanov *[de] and Maha Mostafa[a]

Received 29th August 2023
Accepted 3rd January 2024

DOI: 10.1039/d3ra05885a

rsc.li/rsc-advances

This work examined the influence of zirconium concentration on barium titanate (BZT) $BaZr_xTi_{1-x}O_3$, with (x = 0, 0.15, 0.50, 0.75, and 1), produced by the tartrate precursor technique. The Fourier transform infrared (FTIR) spectra support the X-ray diffraction (XRD) results regarding formation of the perovskite structure. Grain size grows with Zr concentration, suggesting that the presence of Zr ions enlarges the grains. The transmission electron microscopy (TEM) images demonstrated that, due to their nano size, nanocrystallites are agglomerated in most images with irregular morphologies and average particle sizes from 20.75 nm to 63.75 nm. Increasing Zr content diminished the piezoelectric coefficient (d_{33}) and the grain size. The value of d_{33} decreases by increasing Zr content, and there is an inverse relationship between grain size and d_{33}. The remnant polarization of BZT increases with increasing Zr^{4+} content, which may be suitable for permanent memory device applications.

1. Introduction

Barium Zirconate Titanate (BZT) is a significant member of the $BaTiO_3$ family. Much current technology relies on piezoelectric materials. Piezoelectric devices are used in computers; thermistors, capacitors, sensors, and piezoelectric transducers are used in security systems for various applications ranging from tiny speakers to medical ultrasounds.[1–4]

The $BaZr_xTi_{1-x}O_3$ (BZT) are fascinating materials employed as dielectrics in industrial capacitor applications because of their high voltage resistance, dielectric constant, and composition-dependent Curie temperature (T_C). Impurity doping in BZT is a popular method to enhance material performance.[5–9] Several additives are often used with the barium titanate powder to improve performance and maintain appropriate control over the grain sizes and electrical characteristics. Doping $BaTiO_3$ with additions like Sr^{2+}, Ca^{2+}, Sn^{4+}, and Zr^{4+} allows for modifications. Because Zr^{4+} has better chemical stability than Ti^{4+}, doping $BaTiO_3$ with Zr^{4+} can enhance the dielectric and piezoelectric characteristics.

Barium titanate plays a significant role in the design and production of multiferroics. These materials simultaneously have at least two long-range orders in ordering the electronic or spin subsystems.[10] To form multiferroic properties, either the formation of solid solutions[11] or the receiving of composites[12–14] is often used.

The current work aims to prepare $BaZr_xTi_{1-x}O_3$ (x = 0, 0.15, 0.5, 0.75, and 1) nanopowders using tartrate precursor technique and studying the impact of the Zr^{4+} substitution ratio on the morphology, structure, piezoelectric, and ferroelectric characteristics of BZT was examined.

2. Materials and methods

As seen in Fig. 1a, in the synthesis of ferroelectric $BaZr_xTi_{1-x}O_3$ (BZT) materials with varying Zr content (x = 0, 0.15, 0.50, 0.75, and 1) using the tartrate precursor method, a well-defined process comprising several essential steps was meticulously followed. It commenced with the preparation of mixtures of Ba–Zr–Ti solutions, wherein barium nitrate ($Ba(NO_3)_2$), zirconium oxide (ZrO_2), and titanium nitrate ($TiO_2(NO_3)_2$) served as the primary source materials. The precise stoichiometric quantities of these chemicals were carefully determined to correspond with the desired Zr content, as delineated in Table 1. Following the formulation of initial solutions, they underwent 15 minutes of stirring on a hot plate magnetic stirrer. Subsequently, an aqueous solution of tartaric acid ($C_4H_6O_6$) was incorporated into the mixture, ensuring

[a]*Physics Department, Faculty of Science, Tanta University, Al-Geish St., Tanta 31527, Egypt*
[b]*Faculty of Science and Information Technology, Jadara University, Irbid 21110, Jordan*
[c]*Electronic Materials Research Laboratory, Key Laboratory of the Ministry of Education, International Center for Dielectric Research, School of Electronic Science and Engineering, Xi'an Jiaotong University, Xi'an 710049, China*
[d]*Smart Sensors Laboratory, Department of Electronic Materials Technology, National University of Science and Technology MISiS, Moscow, 119049, Russia*
[e]*Laboratory of Magnetic Films Physics, SSPA "Scientific and Practical Materials Research Centre of NAS of Belarus", 19, P. Brovki str., Minsk, 220072, Belarus. E-mail: s.v._trukhanov@gmail.com*

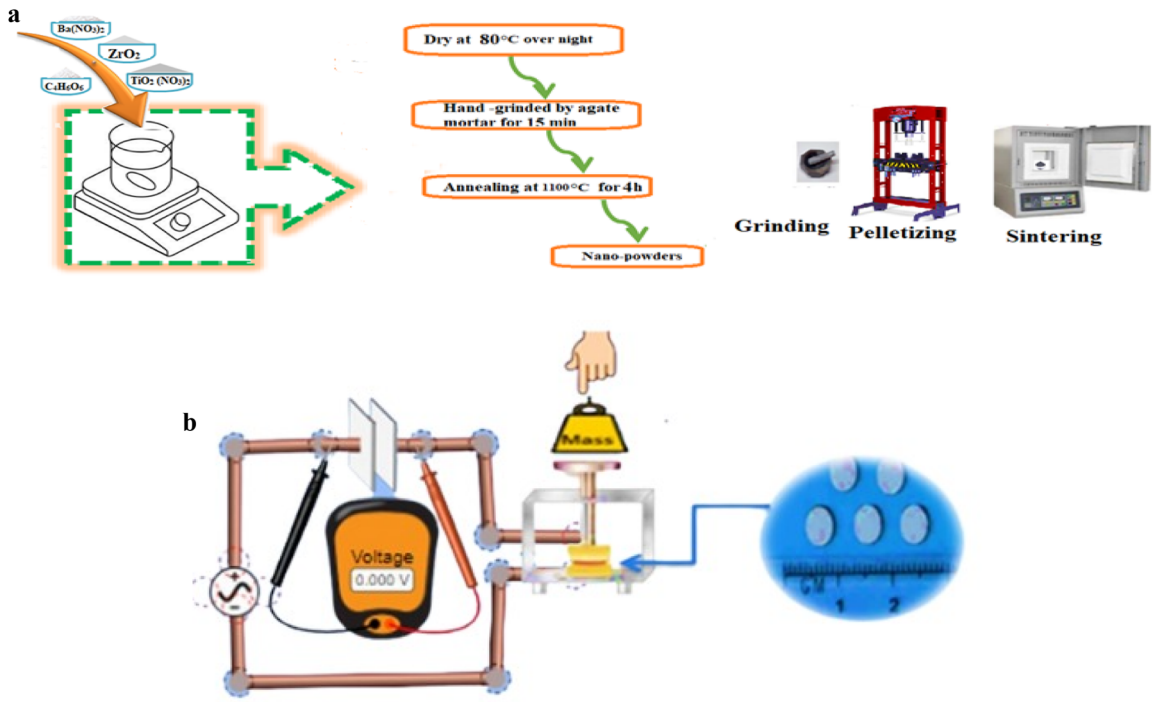

Fig. 1 (a) Samples preparation *via* the tartrate precursor method. (b) The experimental setup of d_{33} measurement.

Table 1 The weights in grams of $BaZr_xTi_{1-x}O_3$

	Weight in grams				
x	$Ba(NO_3)_2$	ZrO_2	TiO_2 $(NO_3)_2$	Molecular weight	Total weight
0.0	26.132	0	20.38756	233.1922	46.51956
0.15	26.132	1.8483	17.329426	239.69575	45.309726
0.50	26.132	6.161	10.19378	254.8707	42.48678
0.75	26.132	9.2415	5.09689	265.70995	40.4703
1.00	26.132	12.322	0	276.5492	38.454

a homogeneous blend with continuous stirring. The subsequent phase involved the gradual evaporation of the solution through heating at a constant temperature of 80 °C while maintaining continuous stirring until reaching a state of dryness. The resulting dried powder was collected and further subjected to drying in a controlled environment at 100 °C. To foster the formation of the desired perovskite structure, the powder was then subjected to annealing at a high temperature of 1100 °C for 4 hours. The final stage of the synthesis process encompassed the pressing of tablets using a compressor, applying a substantial pressure of 5000 kg cm^{-2} while meticulously maintaining the thickness of the resulting tablets at d = 0.35 cm. Detailed records of the weights in grams of the individual chemical components used to synthesize $BaZr_xTi_{1-x}O_3$ for each composition are presented in Table 1. This comprehensive description of the synthesis process and the precision in quantities employed underscores the methodological rigor and consistency in preparing ferroelectric BZT materials with varying Zr content.

This process is a great way to get goods free of impurities at low temperatures. The samples were examined in the 2θ range between 20° and 80° using the X-ray diffraction (XRD) technique (Philips model PW-1729 diffractometer with Cu K_α radiation source with $\lambda = 1.540598$ Å).

The prepared samples' Fourier transform infrared (FTIR) spectra were obtained at room temperature (RT) using a PerkinElmer 1430 instrument in the wavenumber range from 200 cm^{-1} to 4000 cm^{-1}. Transmission electron microscope (TEM) JEOL model 1010 was used to measure the particle size of the produced samples. A JEOL model JSM-5600 scanning electron microscope (SEM) was used to examine the sample morphology. The powders were pressed at 10 Ton into 1.3 cm-diameter discs form. After that, the discs (the pressed prepared samples) were polarized at 2 kV for two hours at RT for piezoelectric tests. By calculating the slope of the charge dependency of the applied stress, which was measured using the circuit in Fig. 1b, the piezoelectric coefficient (d_{33}) was calculated. The Sawyer-Tower circuit has been used to evaluate the samples' ferroelectric hysteresis loop.

3. Results and discussion

3.1. X-ray diffraction and Rietveld refinement analysis

Fig. 2 shows the XRD patterns of the nanocrystalline of BZT annealed at 1100 °C for 4 h. The patterns indicated the tetragonal phase with space group (SG) *P4mm*.[15] The diffraction peaks related to the tetragonal structure are (001), (110), (111), (200), (210), (211), (220), (310), (222) at 2θ = (21.2°, 30.10°, 37.1°, 43.1°, 48.5°, 53.5°, 62.6°, 71°, 75°, 79°) respectively. The sharp and defined peaks of the pattern indicate the high degree crystallinity and main intensity peak (110) increase by increasing Zr content.

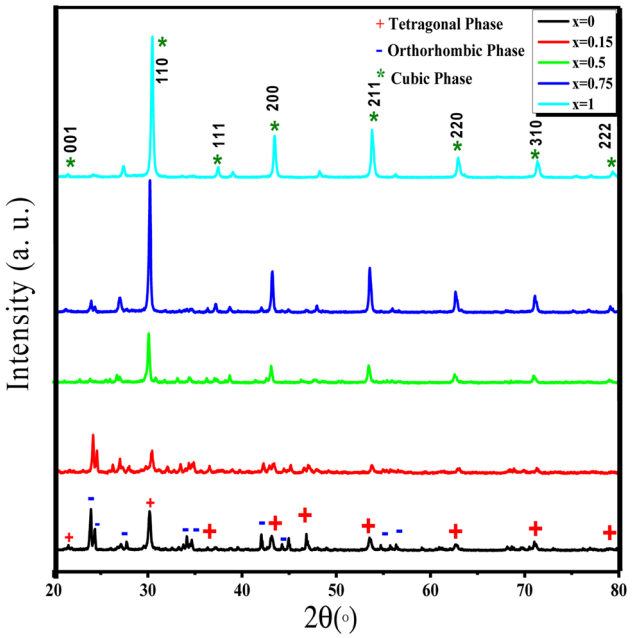

Fig. 2 XRD of $BaZr_xTi_{1-x}O_3$ ($x = 0$, 0.15, 0.50, 0.75, 1).

The Zr ion is considered a non-catalyst agent. It abstracts the reaction process of the perovskite phase, which means that the reaction needs more time and energy for the phase, leading to the increased nanomaterial. The splitting of two diffraction peaks (002) at $2\theta = 43.09°$ and (200) at $2\theta = 44°$ confirm the presence of a tetragonal phase up to $x = 0.75$, whereas the sample $x = 1$ indicates the presence of cubic phase. The phase matching indicates that the tetragonal phase is the predominant one for the samples $x = 0$, 0.15, 0.5, and 0.75. At the same time, $x = 1$ has only a cubic phase.

The last sample has only cubic phase 100%, confirming our discussion. Because the electronic density of the Zr^{+4} ion (ionic radius of 0.72 Å) is higher than that of the Ti^{+4} ion (ionic radius of 0.60 Å), increasing the Zr^{+4} content results in an expansion of the unit cell volume, as shown by the primary diffraction peak (110) shifting to the lower angle side, suggesting an increase in the lattice parameter.[16] The $BaCO_3$ phase appears, and by increasing the Zr content at $x = 0.15$, 0.5, and 0.75, the $BaCO_3$ phase decreases, meaning that annealing the prepared samples at 1100 °C is sufficient for forming perovskite phases with a low percentage of the undesired phases. The tolerance factor is given by the formula:[17]

$$T = \frac{R_A + R_O}{\sqrt{2}(R_B + R_O)}; \quad (1)$$

where R_A, R_B, and R_O are the ionic radius of A and B cations and oxygen ions, respectively. The tolerance factor value should be close to unity for a stable perovskite structure. Tolerance factor values of the samples were calculated using formula (1) and are given in Table 2, where their value range from 0.92 to 0.98,

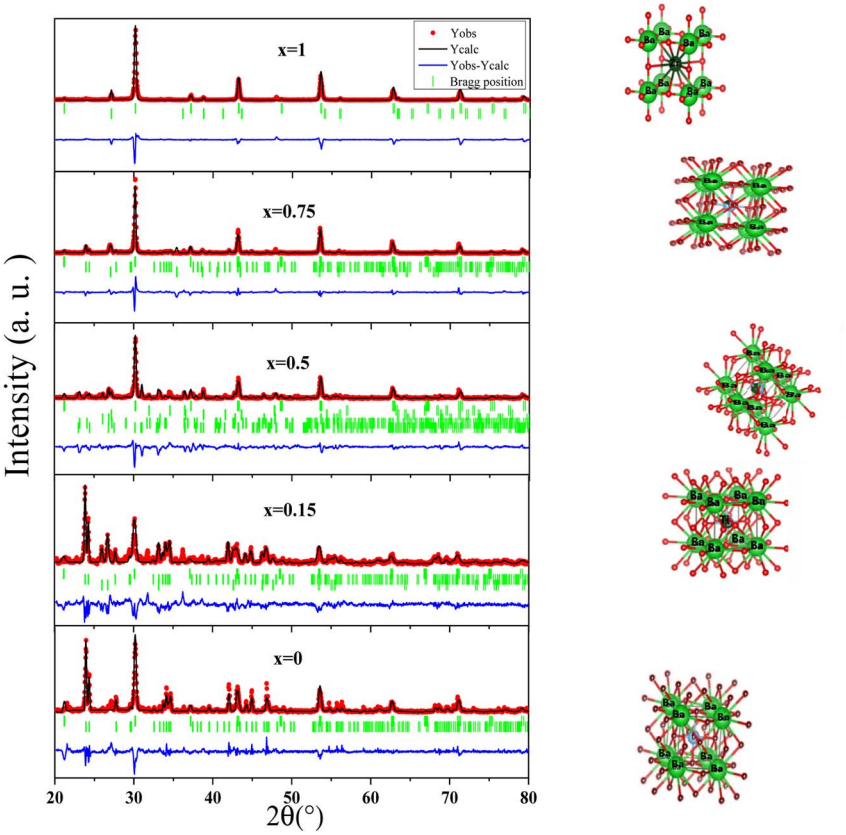

Fig. 3 Rietveld-refined XRD patterns (left) and Rietveld refinement diffraction (right) of $BaZr_xTi_{1-x}O_3$ ($x = 0$, 0.15, 0.5, 0.75, and 1).

Table 2 Tolerance factor and crystallite size of $BaZr_xTi_{1-x}O_3$ ($x = 0$, 0.15, 0.50, 0.75, 1)

x	Tolerance factor	Crystallite size (D) (nm)
0	0.978	28.80
0.15	0.938	17.35
0.50	0.948	33.98
0.75	0.932	41.08
1	0.921	32.66

indicating the decreasing trend with increased Zr content due to the difference in ionic radius of Zr and Ti ions.[18] The tolerance factor is reported to increase when a larger radius cation is substituted in the A-site. In contrast, substituted B-site may decrease the tolerance factor.[4,5]

Scherer's equation is used to figure out the average crystallite size (D) of the perovskite structure:

$$D = \frac{k\lambda}{\beta \cos \theta}; \quad (2)$$

where $k = 0.89$, θ is the position of the diffracted peak, λ is the wavelength of the X-ray source, and β is the full width at half maximum of the peak. The D of the BZT tetragonal phase was calculated and given in Table 2, which increased by increasing Zr content up to $x = 0.75$ and then decreased for the cubic phase $x = 1$.

Fig. 3 shows the Rietveld refinement of $BaZr_xTi_{1-x}O_3$ ($x = 0$, 0.15, 0.5, 0.75, and 1) and indicates the presence of two tetragonal and orthorhombic phases for samples from $x = 0$ up to $x = 0.75$. The tetragonal phases with SG ($P4mm$) have a weight fraction of 48%, 49%, 82%, and 86%, respectively. The orthorhombic phases have a weight fraction of 52%, 51%, 18%, and 14% for all samples $x = 0$–0.75, respectively.

The last sample ($x = 1$ or $BaZrO_3$) has a cubic phase. The analyzed Rietveld refinement values of the tetragonal and orthorhombic phases are given in Table 3, with lattice parameters a, b, and c. It was noticed from Table 3 that for cubic system $a = b = c = 4.18623$ and tetragonal phase $a = b \neq c$. The crystallite size for the two phases is also given in Table 3.

Fig. 3 shows the ball-and-stick model for the tetragonal and cubic phases, which are drawn using the crystallographic information with FullProf and Vesta software. It is shown in Fig. 3 that Ba-ions are in the corners of the unit cell with coordination (0,0,0). In contrast, Ti-ions are in the body center of the unit cell with coordination (0.5,0.5,0.5), as given in Table 4. The O-ions are in the phase center of the tetragonal unit cell. The Rietveld analyzer for sample $x = 1$ (100%) cubic phase with coordination of Ba and Zr ions is present in the body center.[19]

In contrast, the O-ions are at the mid-edge of the unit cell. The lattice parameters, crystallite size, and density of these phases are given in Table 4. The Rietveld refinement of the lattice constant agrees with the above discussion about the weight fraction of the present phases, where $a = b \neq c$ for the tetragonal and $a = b = c$ for the cubic phase.

Table 4 Summary of the ball-and-stick model of $BaZr_xTi_{1-x}O_3$ ($x = 0$, 0.15, 0.5, 0.75, and 1)

		Atomic parameter		
x	Atom	X	Y	Z
0	Ba	0	0	0
	Ti	0.5	0.5	0.49
	O	0.5	0	0.51
0.15	Ba	0	0	0
	Ti	0.5	0.5	0.49
	O	0.5	0	0.51
	Zr	0.5	0.5	0.49
0.50	Ba	0	0	0
	Ti	0.5	0.5	0.45
	O	0.5	0	0.51
	Zr	0.5	0.5	0.45
0.75	Ba	0	0	0
	Ti	0.5	0.5	0.48
	O	0.5	0	0.51
	Zr	0.5	0.5	0.48
1	Ba	0	0	0
	Zr	0.5	0.5	0.5
	O	0.5	0	0

3.2. FTIR analysis

Fig. 4 shows the FTIR spectra for $BaZr_xTi_{1-x}O_3$ where ($x = 0$, 0.15, 0.5, 0.75, and 1). The FTIR spectra showed two principal vibrational absorption bands around 350 cm^{-1} and 548 cm^{-1}; other additional peaks appear at 3394 cm^{-1} due to the existence

Table 3 Summary of Rietveld analyses of XRD data of $BaZr_xTi_{1-x}O_3$ ($x = 0$, 0.15, 0.5, 0.75, and 1)

		Structural parameter							
x	Phase	a (Å)	b (Å)	c (Å)	Crystallographic system	SG	Weight fraction (%)	Density (g cm^{-3})	Crystallite size (nm)
0	$BaTiO_3$	4.185	4.185	4.195	Tetragonal	$P4mm$	48.09	5.269	28.80
	$BaCO_3$	5.307	8.894	6.430	Orthorhombic	$Pmcn$	51.91	4.138	44.56
0.15	$BaZr_{0.15}Ti_{0.85}O_3$	4.193	4.193	4.201	Tetragonal	$P4mm$	49.17	5.387	17.53
	$BaCO_3$	5.320	8.917	6.445	Orthorhombic	$Pmcn$	50.83	4.287	29.83
0.50	$BaZr_{0.5}Ti_{0.5}O_3$	4.178	4.178	4.192	Tetragonal	$P4mm$	81.60	5.783	33.98
	$BaCO_3$	5.583	8.938	6.544	Orthorhombic	$Pmcn$	18.41	4.031	30.09
0.75	$BaZr_{0.75}Ti_{0.25}O_3$	4.182	4.182	4.197	Tetragonal	$P4mm$	85.94	6.008	41.08
	$BaCO_3$	5.303	8.872	6.426	Orthorhombic	$Pmcn$	14.06	4.335	35.27
1	$BaZrO_3$	4.186	4.186	4.186	Cubic	$Pm\bar{3}m$	100	6.259	32.66

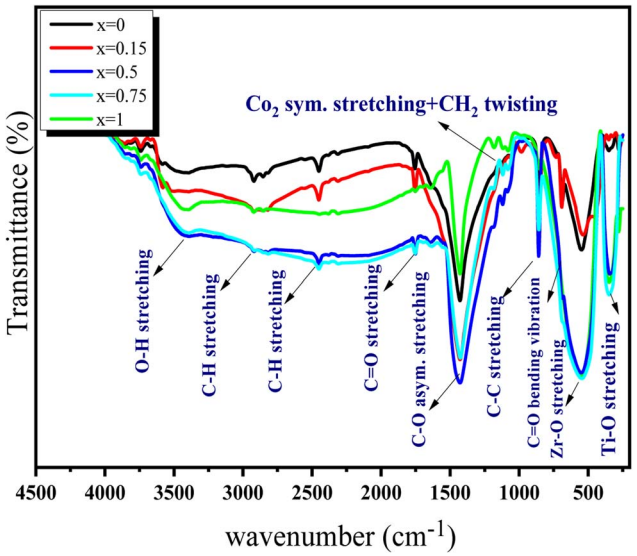

Fig. 4 FTIR spectra of $BaZr_xTi_{1-x}O_3$ ($x = 0$, 0.15, 0.5, 0.75, and 1).

of O–H vibration of water adsorption by the sample, which has an asymmetric stretching mode which increases by increasing Zr content.

Tartaric acid interacts with $BaTiO_3$ during production, as evidenced by a peak at 1428 cm^{-1}, attributed to an asymmetric vibration of the C–O bond.[20] The first two absorption bands are associated with Ti–O stretching and bending vibrational modes. The peak at around 1143 cm^{-1} is attributed to the symmetrical CO_2 and CH_2 twisting mode. The absorption bands at 2464 cm^{-1} and 2927 cm^{-1} are related to the asymmetric and symmetric C–H stretching vibrations of the CH_2 and CH_3 groups, respectively.[21] C–O deformation vibration peaks are around 1428 cm^{-1} and 1168 cm^{-1}. The C–C stretching vibration is linked to the absorption band at 859 cm^{-1}.

Table 5 shows the main frequency bands (ν_1 and ν_2) of $BaZr_xTi_{1-x}O_3$ samples with different amounts of Zr and their force constants (F_1 and F_2). The peaks at 1762 cm^{-1} (C=O stretching vibration), 1438 cm^{-1} (C–O asymmetric stretching vibration), 859 cm^{-1}, and 693 cm^{-1} (C=O bending vibration) all belong to the $BaCO_3$ phase.[22] As x increases from 0 to 0.75, the frequency of the absorption band at 691 cm^{-1} increases before dropping again. The initial absorption band, at 480 cm^{-1}, has the same pattern of activity. By increasing the Zr content, shoulder $\cong$600 cm^{-1}, we may explain this behavior as a modification in the bond length, given that the following equation[23] was used to get the force constant for the A and B sites of the perovskite structure.

3.3. SEM analysis

Fig. 5 displays the morphology of the $BaZr_xTi_{1-x}O_3$ for ($x = 0$, 0.15, 0.5, 0.75 and 1). The presence of Zr ions increases the grain size, as seen by a correlation between grain size and Zr concentration. The upward trend could be attributable to the asymmetry in Zr and Ti ion distribution at the B-site. The SEM graph shows a clear separation in form, supported by the XRD results of the investigated samples, demonstrating an increase in the diffraction peak strength with increasing Zr concentration.[24]

Table 6 shows that increasing grain size results in a higher density. Therefore, the presence of Zr concentration improves densification during sample preparation. Since the average grain size calculated from the SEM micrograph is greater than the crystallite size calculated using Scherer's equation from X-ray analysis, the grain is assumed to be occupancy of crystallites. Indicating that the tetragonal phase expands with both Zr content and grain size, the tetragonality factor c/a rises with increasing Zr concentration.[25] Grains become bigger when Zr ions are replaced with Ti ions, indicating a more stable solid solution in the BaTi lattice.[26]

3.4. TEM analysis

Fig. 6 showcases Transmission Electron Microscopy (TEM) images of Barium Zirconium Titanate ($BaZr_xTi_{1-x}O_3$, abbreviated as BZT) synthesized *via* a tartrate precursor method. This methodology afforded us a series of compositions where zirconium content was systematically varied ($x = 0$, 0.15, 0.5, 0.75, and 1). In conjunction with the quantitative data presented in Table 7, these TEM images reveal a nuanced evolution of nanocrystallite sizes, ranging from 20.75 nm to 63.75 nm. A notable feature observed across multiple frames is the tendency of these nanocrystallites to agglomerate, resulting in irregular morphologies.[15] This phenomenon indicates high surface energy and interaction potential among the nanocrystallites.

The average crystallite size demonstrates a complex dependence on the Zr content. In the absence of Zr ($x = 0$), the size is at its peak, suggesting an inherent stabilizing effect of the Ti-rich matrix. However, as the Zr content increases to $x = 1$, a diminishing trend in size is observed, likely due to the influence of the smaller ionic radius of Zr^{4+} compared to Ti^{4+}. This

Table 5 The values of the main frequencies (ν_1 and ν_2), the force constants (F_1 and F_2), and the bond length of $BaZr_xTi_{1-x}O_3$ ($x = 0$, 0.15, 0.5, 0.75, and 1)

x	ν_2 (cm^{-1})	ν_1 (cm^{-1})	F_2 (dyne per cm) $\times 10^4$	F_1 (dyne per cm) $\times 10^5$	Bond length (Å)
0	351.03	545.81	8.7176	2.1076	2.0961
0.15	351.2	548.05	8.726	2.1249	2.0999
0.50	336.98	541.98	8.0337	2.0781	2.1013
0.75	352.96	553.55	8.8137	2.1678	2.0962
1	348.18	548.79	8.5766	2.1307	____

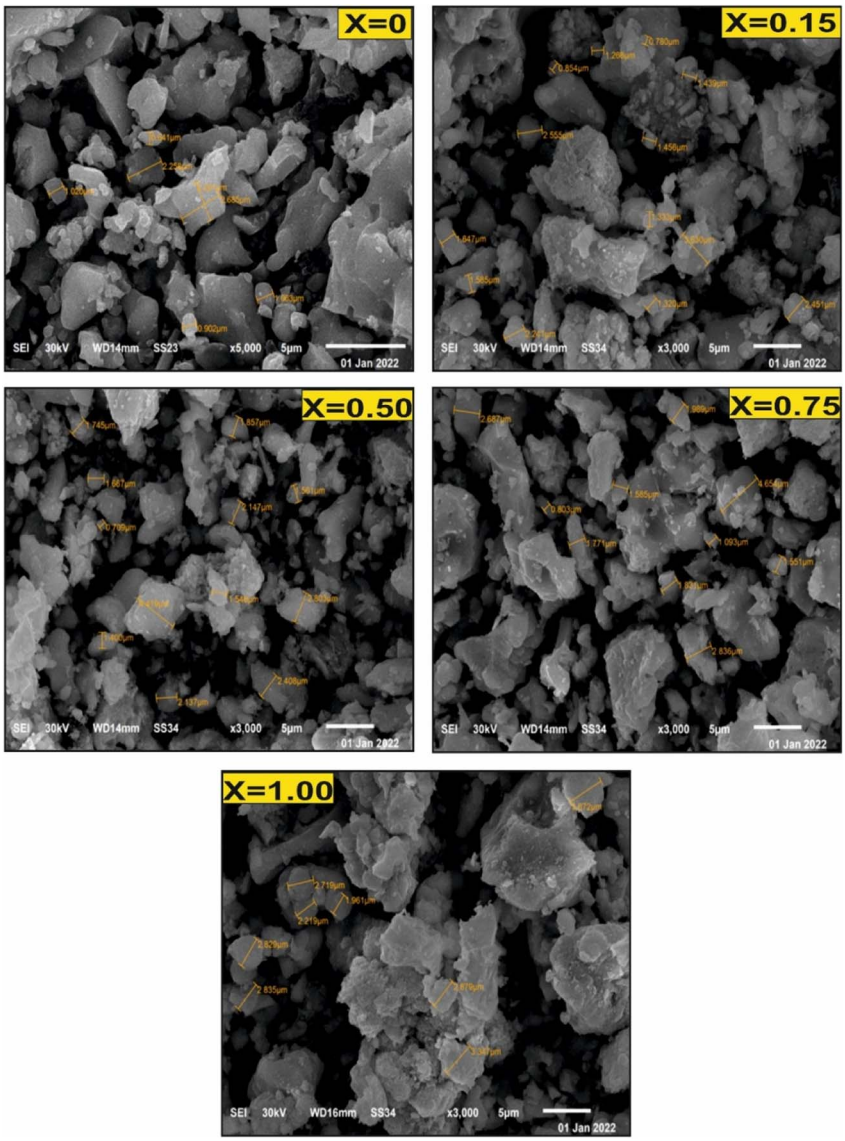

Fig. 5 SEM micrograph of $BaZr_xTi_{1-x}O_3$ (x = 0, 0.15, 0.5, 0.75, and 1).

Table 6 Average grain size, density, crystallite size, and tetragonality factor of $BaZr_xTi_{1-x}O_3$ (x = 0, 0.15, 0.5, 0.75, and 1)

x	Grain size (μm)	Density (g cm^{-3})	Crystallite size (nm)	Tertragonality factor (c/a)
0	1.54	5.269	28.80	1.0025
0.15	1.73	5.387	17.35	1.0018
0.50	1.78	5.783	33.98	1.0034
0.75	2.08	6.008	41.08	1.0035
1	2.80	6.259	32.66	1

size variation is aligned with a phase transition from a predominantly tetragonal structure (up to x = 0.75) to a primarily cubic phase in the final composition (x = 1). This transition is further corroborated by our phase analysis results.

Complementing the TEM analysis, Fig. 6 also presents Selected Area Electron Diffraction (SAED) patterns, crucial for confirming the crystalline nature of the synthesized BZT powders. These patterns reveal a perovskite-type tetragonal structure, which is in harmony with existing literature ref. 15, 27 and 28. The concentric halo rings observed in the electron diffraction patterns distinctly indicate the nanocrystalline nature of the material, with bright spots within these rings signifying high crystallinity. The appearance of these bright spots is a testament to the coherent scattering from well-ordered regions within the material.

Moreover, the SAED analysis provides an accurate delineation of crystalline lattice planes, notably (100), (111), and (210). Identifying these planes finds a direct correspondence in the X-ray diffraction (XRD) patterns, thereby establishing a vital link between SAED and XRD analyses.[29] Our XRD investigations, detailed in Table 7, reveal that the sizes of the tetragonal crystallites are notably larger than those estimated using Scherer's formula. This discrepancy underscores the limitations of

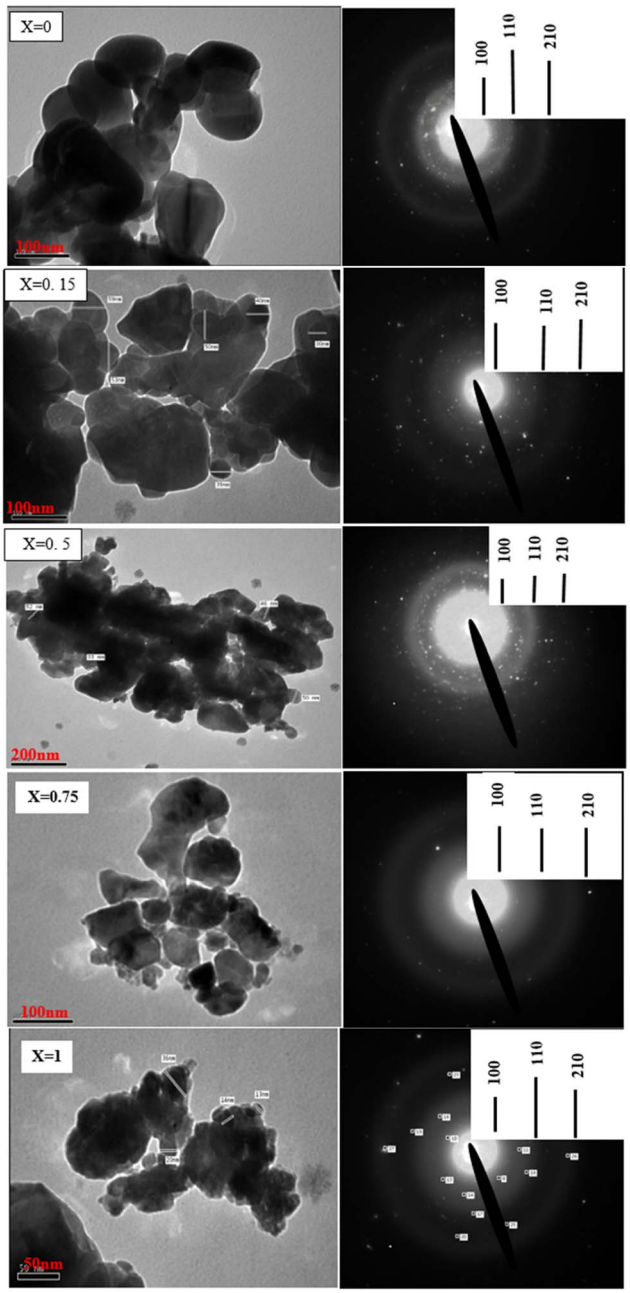

Fig. 6 TEM images of $BaZr_xTi_{1-x}O_3$ ($x = 0$, 0.15, 0.5, 0.75, and 1).

Table 7 Particle, crystallite, and grain size of $BaZr_xTi_{1-x}O_3$ ($x = 0$, 0.15, 0.5, 0.75, and 1)

x	Grain size from SEM (μm)	Particle size from TEM (nm)	Crystallite size from XRD (nm)
0	1.54	28	28.80
0.15	1.73	63.75	17.53
0.50	1.78	45.25	33.98
0.75	2.08	40	41.08
1	2.80	20.75	32.66

Scherer's formula, particularly in resolving smaller crystal sizes, as the lower detection limit of our XRD instrument stands at 20.75 nm.

Lastly, the efficacy of the tartrate precursor technique in yielding a nanocrystalline perovskite phase is amply demonstrated in the TEM images. These images show the crystallites' tetragonal shape and their transition to a cubic shape in the final composition ($x = 1$), mirroring the phase transition observed in XRD analysis. This alignment between morphological and crystallographic data underscores the intricate interplay between composition, crystal structure, and morphology in the BZT system.

3.5. Piezoelectric coefficient

Fig. 7 shows the impact of applied force on the produced samples' piezoelectric charge (Q_{33}). It was found that the Q_{33} of the polarized sample declined as the applied stress increased, and we can compute the d_{33} in the unit (PC/N) from the slope of this line. The rotation of the 90° and 180° domains caused by an external electric field gives birth to the piezoelectric response.[23,29,30] The d_{33} calculated values for all synthesized samples are shown in Table 8. It is noticed that the value of d_{33} decreases by increasing Zr content. The value of d_{33} is affected by the domain wall motion and the grain size, where the sample with a large grain size has lower piezoelectricity (d_{33}), as given in Table 8.

Another aspect that influences the value of d_{33} is the tetragonality factor (c/a),[23] which increases by increasing Zr content and is higher for sample $x = 0.75$ and equal to 1.047, as given in Table 8. Generally, the piezoelectric constant is correlated by the crystal structure, grain size, and density. The grain size has the most significant impact on the piezoelectric constant. The coupling effect between borders increases as grain size increases, producing a drop in domain mobility and polarization and, ultimately, a decrease in d_{33}. It is essential to say the piezoelectric properties are strongly affected by the preparation

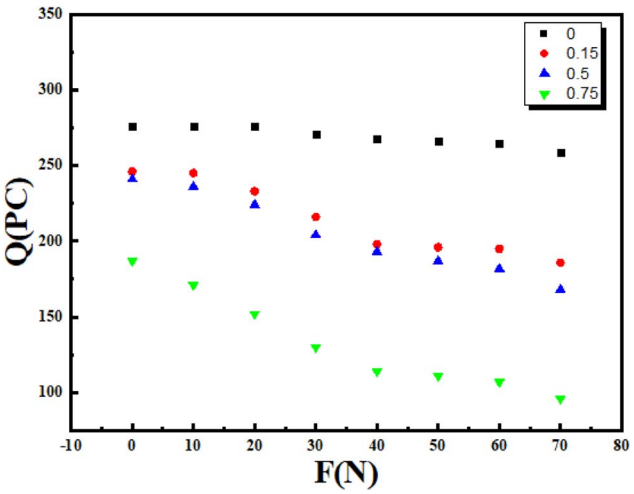

Fig. 7 The piezoelectric charge Q_{33} of the BZT samples for different Zr content.

Table 8 The values of d_{33}, grain size, tetragonality factor, and crystalline size for different Zr content

Sample	d_{33} (PC/N)	Grain size (μm)	Tetragonality factor (c/a)	Crystalline size (nm)	Reference
$BaTiO_3$	10.08	1.54	1.0025	28.80	Present work
$BaZr_{0.15}Ti_{0.75}O_3$	8.30	1.73	1.0018	17.53	
$BaZr_{0.50}Ti_{0.50}O_3$	7.94	1.78	1.0034	33.98	
$BaZr_{0.75}Ti_{0.25}O_3$	6.76	2.08	1.0035	41.08	
$BaZrO_3$	—	2.80	1	32.66	
$BaTiO_3$	31.1	—	—	—	30
$BaTiO_3$	45	—	—	—	31
EVA/$BaTiO_3$	0.85	—	—	—	32
$BaTiO_3$/PVDF	18	—	—	—	33
BZT-BCT	10	—	—	—	34
BFZT-BT	19	—	—	—	35

method and the type of raw materials, which affect the grain size and the piezoelectric properties.[31–33] As seen in Table 8, there is an inverse relationship between grain size and d_{33}. The sample $x = 1$ deviates from the above discussion when the crystal structure is cubic. In the context of our research, we have clarified a fundamental relationship between grain size and the piezoelectric coefficient (d_{33}). It is worth noting that grain size typically surpasses particle size in the hierarchical structure of the material. This phenomenon arises because an individual grain may encompass multiple agglomerated particles. Within this structural framework, an individual particle can exhibit the characteristics of a single, perfect crystal. In such cases, the dimensions of this particle align with what we call the crystallite size. However, a key consideration emerges when a particle presents certain low-angle defects, such as stacking faults or twin defects, which can reduce crystallite size. This parameter, reflecting the region characterized by perfect crystalline order, is routinely determined through X-ray diffraction (XRD) and consistently yields values smaller than those observed using electron microscopy.

A fundamental observation in our study is the discernment of an inversely proportional relationship between grain size and the piezoelectric coefficient (d_{33}). Notably, this relationship is underscored by the empirical finding that larger grain sizes correspond to lower d_{33} values. This discernment emphasizes grain size's considerable impact on the material's piezoelectric behavior. In light of the pivotal role played by grain size in influencing d_{33}, our investigation underscores the significance of understanding these structural parameters in the context of piezoelectric materials. Our result is in agreement with the previous work.[34]

3.6. The ferroelectric hysteresis-loop of BZT samples

Fig. 8 denotes the RT *P–E* hysteresis loops for BZT samples. It is observed that the inclination of the hysteresis loop increases by increasing zirconium content up to sample $x = 0.75$ when sample $x = 0$ has a minimum inclination.[36] The polarization increase for sample $x = 0.75$ due to the increase of 180° and 90° domains in the direction of the applied field.[37] The remnant polarization was increased by increasing content up to $x = 0.75$, indicating that the Zr is a well-selected material for alignment for the domain of BZT samples,[38] suggesting that the studied ferroelectric samples are relaxors ferroelectrics with soft hysteresis loops as shown in Table 9. At RT, all the present hysteresis loops for samples $x = 0$, 0.15, and 0.5 show relaxer

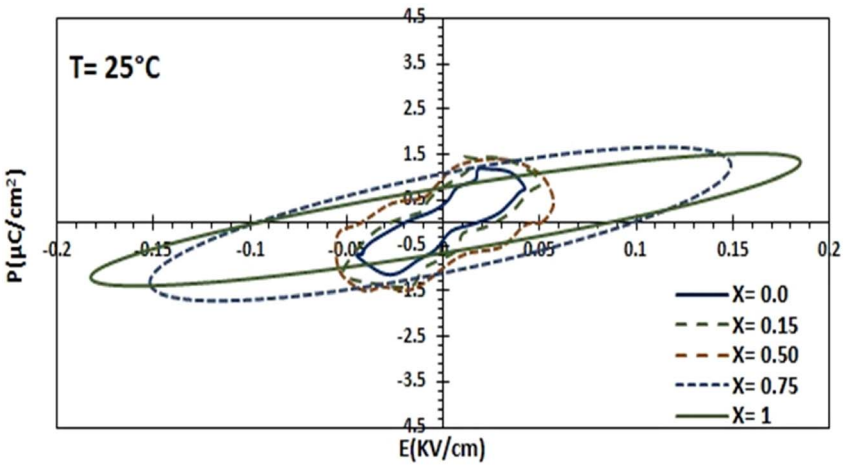

Fig. 8 The *P–E* hysteresis loops of $BaZr_xTi_{1-x}O_3$ samples where x = (0, 0.15, 0.5, 0.75, and 1).

Table 9 Ferroelectric parameters of $BaZr_xTi_{1-x}O_3$ samples where x = (0, 0.15, 0.5, 0.75, and 1)

Composition (x)	E_c (kV cm^{-1})	P_r (μ_c cm^{-2})	P_s (μ_c cm^{-2})
0	0.02	0.4	1
0.15	0.03	0.7	1.5
0.5	0.05	0.8	1.45
0.75	0.1	1	1.6
1	0.09	0.7	1.4

ferroelectric behavior;[39] these disordered hysteresis loops could be obeying the domain to is the relaxor material up to the applied field.[40]

4. Conclusions

$BaZr_xTi_{1-x}O_3$ samples with various Zr contents ($x = 0$, 0.15, 0.50, 0.75, and 1) were prepared using the tartrate precursor approach. According to the phase matching, the tetragonal phase predominates for samples with $x = 0$, 0.15, 0.5, and 0.75, whereas $x = 1$ only possesses a cubic phase. The crystallite size grew when the Zr content was raised to $x = 0.75$. When $x = 1$ was reached, the size was reduced. Ti ions are located in the cell's body center. In contrast, Ba-ions are at the corners of the unit cell with coordination (0,0,0) and (0.5,0.5,0.5), respectively. The sintering temperature of perovskite BZT powder is confirmed to be over 1100 °C by the compatibility of FTIR spectra with XRD investigation. Ti-ions replace Zr-ions to provide a more stable solid solution in the BaTi-lattice, which promotes grain enlargement. Zr is a well-selected material for alignment for the domain of BZT samples since the value of d_{33} declines with increasing Zr content and concentration up to $x = 0.75$, increasing residual polarization. The comprehensive approach, combining the tartrate precursor synthesis with extensive structural and functional analyses, has elucidated the complex interplay between Zr doping, crystal structure, grain size, and piezoelectric properties in BZT. This study advances our understanding of the material properties of doped barium titanates. It paves the way for developing novel ferroelectric materials with tailored properties for specific applications.

Author contributions

Conceptualization, M. M. S., O. M. H., M. A. D., E. L. T., A. V. T., S. V. T., and M. M.; methodology, M. M. S., A. M. A., Y. A. A., R. G., M. A. D., and M. M.; validation, M. M. S., A. M. A., Y. A. A., R. G., M. K., M. U. K., and O. M. H.; formal analysis, O. M. H., D. Z., M. A. D., E. L. T., M. K., M. U. K., A. V. T., and S. V. T.; investigation, A. M. A., Y. A. A., R. G., E. L. T., A. V. T., and S. V. T.; resources, O. M. H., Z. D., E. L. T., A. V. T., and S. V. T.; data curation, Z. D., M. A. D., E. L. T., A. V. T., and S. V. T.; writing—original draft preparation, M. M. S., E. L. T., A. V. T., S. V. T., and M. M.; writing—review and editing, M. M. S., E. L. T., A. V. T., S. V. T., and M. M.; visualization, A. M. A., Y. A. A., R. G., O. M. H., M. K., M. U. K., and M. A. D.; supervision, A. V. T., S. V. T., and M. M.; project administration, M. A. D., E. L. T., A. V. T., S. V. T., and M. M.; funding acquisition, M. A. D., E. L. T., M. K., M. U. K., A. V. T., and S. V. T. All authors have read and agreed to the published version of the manuscript.

Conflicts of interest

The authors declare no conflict of interest.

Acknowledgements

Alex V. Trukhanov thanks NUST MISIS for support within the framework of the "Priority 2030" (Smart Sensors Laboratory—project K6-2022-043).

References

1 M. M. Hessien, N. El-Bagoury, M. H. H. Mahmoud and O. M. Hemeda, Synthesis and characterization of nanocrystalline barium-samarium titanate, *High Temp. Mater. Processes*, 2016, **35**, 499–505, DOI: **10.1515/htmp-2015-0021**.

2 A. Prasatkhetragarn, T. Sareein, N. Triamnak and R. Yimnirun, Dielectric and ferroelectric properties of modified-BaTiO3 lead-free ceramics prepared by solid solution method, *Ferroelectrics*, 2022, **586**, 224–241, DOI: **10.1080/00150193.2021.2014274**.

3 C. Filipič, Z. Kutnjak, R. Pirc, G. Canu and J. Petzelt, BaZr0.5Ti0.5O3: lead-free relaxor ferroelectric or dipolar glass, *Phys. Rev. B*, 2016, **93**, 224105, DOI: **10.1103/PhysRevB.93.224105**.

4 T. Maiti, R. Guo and A. S. Bhalla, Evaluation of experimental resume of BaZrxTi1-xO3 with perspective to ferroelectric relaxor family: an overview, *Ferroelectrics*, 2011, **425**, 4–26, DOI: **10.1080/00150193.2011.644168**.

5 M. Aamir, I. Bibi, S. Ata, K. Jilani, F. Majid, S. Kamal, N. Alwadai, M. A. S. Raza, M. Bashir, S. Iqbal, M. Aadil and M. Iqbal, Ferroelectric, dielectric, magnetic, structural and photocatalytic properties of Co and Fe doped LaCrO3 perovskite synthesized *via* micro-emulsion route, *Ceram. Int.*, 2021, **47**, 16696–16707, DOI: **10.1016/j.ceramint.2021.02.240**.

6 S. B. Li, C. B. Wang, X. Ji, Q. Shen and L. M. Zhang, Effect of composition fluctuation on structural and electrical properties of BZT-xBCT ceramics prepared by Plasma Activated Sintering, *J. Eur. Ceram. Soc.*, 2017, **37**, 2067–2072, DOI: **10.1016/j.jeurceramsoc.2016.12.043**.

7 Z. Liu, R. Yuan, D. Xue, W. Cao and T. Lookman, Origin of large electrostrain in Sn4+ doped Ba(Zr0.2Ti0.8)O3-x(Ba0.7Ca0.3)TiO3 ceramics, *Acta Mater.*, 2018, **157**, 155–164, DOI: **10.1016/j.actamat.2018.07.004**.

8 S. Ke, H. Fan, H. Huang, H. L. W. Chan and S. Yu, Dielectric dispersion behavior of Ba(ZrxTi1-x)O3 solid solutions with a quasiferroelectric state, *J. Appl. Phys.*, 2008, **104**, 034108, DOI: **10.1063/1.2964088**.

9 C. Zhang, Z. Zhou, Z. Tang, D. Ballo, C. Wang and G. Jian, Effects of scandium oxide on domain structure, dielectric

and ferroelectric properties of barium zirconate titanate ceramics, *J. Alloys Compd.*, 2022, **889**, 161622, DOI: 10.1016/j.jallcom.2021.161622.

10 V. Turchenko, A. S. Bondyakov, S. Trukhanov, I. Fina, V. V. Korovushkin, M. Balasoiu, S. Polosan, B. Bozzo, N. Lupu and A. Trukhanov, Microscopic mechanism of ferroelectric properties in barium hexaferrites, *J. Alloys Compd.*, 2023, **931**, 167433, DOI: 10.1016/j.jallcom.2022.167433.

11 D. V. Karpinsky, M. V. Silibin, S. V. Trukhanov, A. V. Trukhanov, A. L. Zhaludkevich, S. I. Latushka, D. V. Zhaludkevich, V. A. Khomchenko, D. O. Alikin, A. S. Abramov, T. Maniecki, W. Maniukiewicz, M. Wolff, V. Heitmann and A. L. Kholkin, Peculiarities of the crystal structure evolution of BiFeO3–BaTiO3 ceramics across structural phase transitions, *Nanomaterials*, 2020, **10**, 801, DOI: 10.3390/nano10040801.

12 S. V. Trukhanov, A. V. Trukhanov, M. M. Salem, E. L. Trukhanova, L. V. Panina, V. G. Kostishyn, M. A. Darwish, An. V. Trukhanov, T. I. Zubar, D. I. Tishkevich, V. Sivakov, D. A. Vinnik, S. A. Gudkova and C. Singh, Preparation and investigation of structure, magnetic and dielectric properties of (BaFe11.9Al0.1O19)1-x - (BaTiO3)x bicomponent ceramics, *Ceram. Int.*, 2018, **44**, 21295–21302, DOI: 10.1016/j.ceramint.2018.08.180.

13 M. M. Salem, L. V. Panina, E. L. Trukhanova, M. A. Darwish, A. T. Morchenko, T. I. Zubar, S. V. Trukhanov and A. V. Trukhanov, Structural, electric and magnetic properties of (BaFe11.9Al0.1O19)1-x - (BaTiO3)x composites, *Composites, Part B*, 2019, **174**, 107054–107058, DOI: 10.1016/j.compositesb.2019.107054.

14 R. E. El-Shater, A. S. Atlam, M. K. Elnimr, S. T. Assar, S. V. Trukhanov, D. I. Tishkevich, T. I. Zubar, A. V. Trukhanov, D. Zhou and M. A. Darwish, AC measurements, impedance spectroscopy analysis, and magnetic properties of Ni0.5Zn0.5Fe2O4/BaTiO3 multiferroic composites, *Mater. Sci. Eng., B*, 2022, **286**, 116025, DOI: 10.1016/j.mseb.2022.116025.

15 T. Badapanda, S. Sarangi, B. Behera, P. K. Sahoo, S. Anwar, T. P. Sinha, G. E. Luz, E. Longo and L. S. Cavalcante, Structural refinement, optical and ferroelectric properties of microcrystalline Ba(Zr0.05Ti0.95)O3 perovskite, *Curr. Appl. Phys.*, 2014, **14**, 708–715, DOI: 10.1016/j.cap.2014.02.015.

16 C. Ostos, L. Mestres, M. L. Martínez-Sarrión, J. E. García, A. Albareda and R. Perez, Synthesis and characterization of A-site deficient rare-earth doped BaZrxTi1-xO3 perovskite-type compounds, *Solid State Sci.*, 2009, **11**, 1016–1022, DOI: 10.1016/j.solidstatesciences.2009.01.006.

17 A. M. A. Henaish, O. M. Hemeda, A. M. Dorgham and M. A. Hamad, Characterization of excessive Sm3+ containing barium titanate prepared by tartrate precursor method, *J. Mater. Res. Technol.*, 2020, **9**, 15214–15221, DOI: 10.1016/j.jmrt.2020.10.015.

18 N. Vonrüti and U. Aschauer, Band-gap engineering in AB(OxS1-x)3 perovskite oxysulfides: a route to strongly polar materials for photocatalytic water splitting, *J. Mater. Chem. A*, 2019, **7**, 15741–15748, DOI: 10.1039/c9ta03116b.

19 P. Sateesh, J. Omprakash, G. S. Kumar and G. Prasad, Studies of phase transition and impedance behavior of Ba(Zr,Ti)O3 ceramics, *J. Adv. Dielectr.*, 2015, **5**, 1550002, DOI: 10.1142/S2010135X15500022.

20 N. Chakrabarti and H. S. Maiti, Chemical synthesis of barium zirconate titanate powder by an autocombustion technique, *J. Mater. Chem.*, 1996, **6**, 1169–1173, DOI: 10.1039/jm9960601169.

21 O. M. Hemeda, M. E. A. Eid, T. Sharshar, H. M. Ellabany and A. M. A. Henaish, Synthesis of nanometer-sized PbZrxTi1-xO3 for gamma-ray attenuation, *J. Phys. Chem. Solids*, 2021, **148**, 109688, DOI: 10.1016/j.jpcs.2020.109688.

22 T. Thananatthanachon, Synthesis and characterization of a perovskite barium zirconate (BaZrO3): an experiment for an advanced inorganic chemistry laboratory, *J. Chem. Educ.*, 2016, **93**, 1120–1123, DOI: 10.1021/acs.jchemed.5b00924.

23 O. M. Hemeda, B. I. Salem, H. Abdelfatah, G. Abdelsatar and M. Shihab, Dielectric and ferroelectric properties of barium zirconate titanate ceramics prepared by ceramic method, *Phys. B*, 2019, **574**, 411680, DOI: 10.1016/j.physb.2019.411680.

24 P. S. Aktaş, Structural investigation of barium zirconium titanate Ba(Zr0.5Ti0.5)O3 particles synthesized by high energy ball milling process, *J. Chem. Sci.*, 2020, **132**, 3–10, DOI: 10.1007/s12039-020-01837-7.

25 M. Reda, S. I. El-Dek and M. M. Arman, Improvement of ferroelectric properties *via* Zr doping in barium titanate nanoparticles, *J. Mater. Sci.: Mater. Electron.*, 2022, **33**, 16753–16776, DOI: 10.1007/s10854-022-08541-x.

26 N. Binhayeeniyi, P. Sukvisut, C. Thanachayanont and S. Muensit, Physical and electromechanical properties of barium zirconium titanate synthesized at low-sintering temperature, *Mater. Lett.*, 2010, **64**, 305–308, DOI: 10.1016/j.matlet.2009.10.069.

27 H. H. Huang, H. H. Chiu, N. C. Wu and M. C. Wang, Tetragonality and properties of Ba(ZrxTi1-x)O3 ceramics determined using the Rietveld method, *Metall. Mater. Trans. A*, 2008, **39**, 3276–3282, DOI: 10.1007/s11661-008-9622-2.

28 O. M. Hemeda, B. I. Salem, H. Abdelfatah, G. Abdelsatar and M. Shihab, Dielectric and ferroelectric properties of barium zirconate titanate ceramics prepared by ceramic method, *Phys. B*, 2019, **574**, 411680, DOI: 10.1016/j.physb.2019.411680.

29 A. M. Henaish, M. Mostafa, I. Weinstein, O. Hemeda and B. Salem, Ferroelectric and dielectric properties of strontium titanate doped with barium, *Magnetism*, 2021, **1**, 22–36, DOI: 10.3390/magnetism1010003.

30 A. Tawfik, Elastic properties and sound wave velocity of PZT transducers doped with Ta and La, *J. Am. Ceram. Soc.*, 1985, **68**, 317–319, DOI: 10.1111/j.1151-2916.1985.tb10132.x.

31 P. Zheng, J. L. Zhang, Y. Q. Tan and C. L. Wang, Grain-size effects on dielectric and piezoelectric properties of poled

BaTiO3 ceramics, *Acta Mater.*, 2012, **60**, 5022–5030, DOI: **10.1016/j.actamat.2012.06.015**.

32 Y. Huan, X. Wang, J. Fang and L. Li, Grain size effects on piezoelectric properties and domain structure of BaTiO3 ceramics prepared by two-step sintering, *J. Am. Ceram. Soc.*, 2013, **96**, 3369–3371, DOI: **10.1111/jace.12601**.

33 V. R. Mudinepalli, L. Feng, W. C. Lin and B. S. Murty, Effect of grain size on dielectric and ferroelectric properties of nanostructured Ba0.8Sr0.2TiO3 ceramics, *J. Adv. Ceram.*, 2015, **4**, 46–53, DOI: **10.1007/s40145-015-0130-8**.

34 H. Shokrollahi, F. Salimi and A. Doostmohammadi, The fabrication and characterization of barium titanate/akermanite nano-bio-ceramic with a suitable piezoelectric coefficient for bone defect recovery, *J. Mech. Behav. Biomed. Mater.*, 2017, **74**, 365–370, DOI: **10.1016/j.jmbbm.2017.06.024**.

35 M. B. Ghasemian, Q. Lin, E. Adabifiroozjaei, F. Wang, D. Chu and D. Wang, Morphology control and large piezoresponse of hydrothermally synthesized lead-free piezoelectric $(Bi_{0.5}Na_{0.5})TiO_3$ nanofibres, *RSC Adv.*, 2017, **7**, 15020–15026, DOI: **10.1039/c7ra01293d**.

36 X. Li, M. Sun, X. Wei, C. Shan and Q. Chen, 1D piezoelectric material based nanogenerators: methods, materials and property optimization, *Nanomaterials*, 2018, **8**, 188, DOI: **10.3390/nano8040188**.

37 O. Zahhaf, G. D'Ambrogio, A. Giunta, M. Q. Le, G. Rival, P. J. Cottinet and J. F. Capsal, Molten-State Dielectrophoretic Alignment of EVA/$BaTiO_3$ Thermoplastic Composites: Enhancement of Piezo-Smart Sensor for Medical Application, *Int. J. Mol. Sci.*, 2022, **23**, 15745, DOI: **10.3390/ijms232415745**.

38 Z. Wang, L. Wang, Y. Meng, Y. Wen and J. Pei, Effects of Conductive Carbon Black on Thermal and Electrical Properties of Barium Titanate/Polyvinylidene Fluoride Composites for Road Application, *J. Renewable Mater.*, 2023, **11**, 2469–2489, DOI: **10.32604/jrm.2023.025497**.

39 S. A. Riquelme, K. Ramam and A. F. Jaramillo, Ceramics fillers enhancing effects on the dielectric properties of poly(vinylidene fluoride) matrix composites prepared by the torque rheometer method, *Results Phys.*, 2019, **15**, 102800, DOI: **10.1016/j.rinp.2019.102800**.

40 X. Shan, C. Zhou, Z. Cen, H. Yang, Q. Zhou and W. Li, $Bi(Zn_{1/2}Ti_{1/2})O_3$ modified $BiFeO_3$-$BaTiO_3$ lead-free piezoelectric ceramics with high temperature stability, *Ceram. Int.*, 2013, **39**, 6707–6712, DOI: **10.1016/j.ceramint.2013.01.110**.